Optimization of laser beam welding of steel parts made by additive manufacturing

Fabrizia Caiazzo [1] · Vittorio Alfieri [1]

Abstract

To pursue all the benefits of additive manufacturing of metals, recent studies have been aimed at assessing a proper welding technology to obtain large products by means of joining smaller parts. Indeed, at present, two or more parts must be manufactured individually and then assembled to produce the final component, when the size is incompatible with the building chamber or severe deformations arise during building. In this paper, laser beam welding is explored to join stainless steel components made by the process of laser powder bed fusion, in order to benefit from all the known advantages of this joining technique, aiming at producing a welding bead with homogeneous mechanical features with respect to the unwelded counterpart: a factorial plan is built, and the response surfaces are presented; then, the consolidated method of the desirability function is used to find the optimum condition of welding with reference to the current international standards, taking into account the geometry, the welding imperfections, and the extent of the heat-affected zone. The suggested optimum is eventually assessed via tensile testing and compared to the unwelded sample.

1 Introduction

Additive manufacturing (AM) techniques are based on the principle of layer-upon-layer fabrication of the parts, as opposed to subtractive manufacturing methods [1]. The opportunity of deep customization of complex products is well-documented [2], and the increasing offer of available materials is a leading factor contributing to the diffusion of AM in many industrial fields [3].

At present, AM has moved from the fabrication of prototypes to functional metal parts, aiming at direct mechanical applications. In this frame, laser powder bed fusion (LPBF) and electron beam melting (EBM) are the main technologies to process a wide range of metal alloys [4]. Near-full-density objects can be manufactured starting from loose powder, even for industrial fields where strict standards apply, such in aerospace and automotive [5, 6]. Moreover, redesign is usually performed prior to building [7], aiming at lightweight parts, with conformal channels for cooling, which are not feasible with conventional manufacturing processes. A significant reduction of costs and waste is documented; a favorable buy-to-fly ratio is benefited.

Nevertheless, a drawback must be addressed, because the direct fabrication of a large component is not feasible in general as monolithic, due to the limited size of the building chamber in commercial AM equipment. The issue is more crucial in case of metals, because increasing the size of LPBF or EBM machines is challenging and expensive, due to the need for accurate calibration of the electron or laser beam over larger areas and controlled atmosphere or vacuum to prevent oxidation [8, 9]. Moreover, heating and cooling cycles during building usually result in residual stresses which are more severe on large parts and may lead to possible fracture under loading [10].

Consequently, a possible solution is to manufacture two or more AM-made parts individually and then assemble them, to produce a larger final component, with theoretically no dimensional limitations. Evidently, the current challenge is to offer homogeneous mechanical features with respect to the monolithic hypothetical counterpart.

Many options for joining metals are available in the literature depending on the chemical composition, the thickness of

✉ Vittorio Alfieri
valfieri@unisa.it

[1] Department of Industrial Engineering, University of Salerno, Via Giovanni Paolo II 132, 84084 Fisciano, Italy

the part, and the final application; nevertheless, the feasibility and effectiveness of each technology of joining are a subject of debate in case of parts obtained via LPBF or AM in general: firstly, because any method must allow design flexibility to preserve the advantages of AM, and secondly, because the microstructure upon AM is significantly different from the wrought or casted material of the same chemical composition [11]. In general, a peculiar fine grain structure results from LPBF [12] or EBM and must be preserved; otherwise, the mechanical properties are degraded. Traditional arc welding yields coarser microstructure in the welding bead with respect to the base material, unless a post-process heat treatment is performed. Friction stir welding is a valid solution instead, being it a solid-state method: it is usually suggested for alloys which are prone to cracking and formation of brittle secondary phases upon fusion and solidification [13]; it has been successfully implemented for Al-based [14] and Ti-based [8] alloys produced via LPBF. Nevertheless, flexibility over complex shapes is still an issue.

At present, interest is growing towards flexible methods such as electron beam welding (EBW) and laser beam welding (LBW): in both cases, a focused energy source is delivered to the parts, allowing to reduce the heat-affected zones to the order of few tenths of millimeters; reduced distortion of the components is also benefited [15]. Moreover, the welding efficiency is higher compared to conventional methods [16], and downloading of information to the purpose of monitoring and online control is possible [17]. Thanks to steeper cooling rates, a fine microstructure is produced in the welding bead, and the mechanical properties resulting from LPBF are potentially saved. Therefore, both EBW and LBW have been proposed in the literature to join parts obtained with LPBF, namely, EBW for Al-based [18] and Ti-based [19] alloys and LBW for steel [20, 21], Ti-based [22, 23], and Ni-based [24] alloys.

This paper is aimed at further exploring the well-known advantages of butt LBW, considering steel parts obtained with LPBF. Some authors addressed it in T-joint configuration [20], although they specifically focused on the influence of the heat treatment before welding, some in butt-joint configuration [21] to compare the outcome with wrought sheets. Instead, an optimization of welding is offered in this paper, with a proper assessment of the weld quality in terms of seam geometry with respect to applicable standards for laser welding, aiming at reducing any possible discontinuity induced by the welding bead over the mechanical features.

To this purpose, a structured experimental plan must be arranged, since many governing factors are involved in LBW [16]. A sensible choice is required to select the main factors to investigate. Laser power and speed are crucial because these define the energy input; in addition, the effect of defocusing, which has been neglected in a similar work in the literature [21], has been considered in this paper, being it

crucial to the stability of the key-hole [16]. It has been reported that even the angle of the laser beam is significant [9, 25], for steel in particular [26], since underfilling and spattering are affected; nevertheless, tilting of the laser head may not be viable in actual application over complex geometries of certain AM parts; therefore, this possibility has not been investigated here.

The responses to set the constraints for optimization have been defined in agreement with the literature and are mainly related to the size of the fusion zone [25]; the effectiveness of the outcome has been discussed with respect to the usual international standards for welding [27]. The consolidated method of the desirability function has been used to find the optimum condition of processing. Eventually, tensile testing has been performed, and the outcome has been compared with the unwelded AM counterpart.

2 Experimental procedure

2.1 Additive manufacturing via LPBF

Commercial pre-alloyed nitrogen-atomized EOS GP1 powder with 36-µm mean grain size has been considered (Fig. 1), with nominal chemical composition matching the 17-4 precipitation hardenable stainless steel, according to UNS S17400 standard (Table 1); the choice of the base metal is based on potential applications, thanks to a favorable combination of mechanical strength, wear resistance, and corrosion resistance [7].

The specimens to be welded, 60 mm wide and large and 3 mm thick, have been manufactured in nitrogen atmosphere, with residual oxygen content below 1%, using a commercial EOS M270 laser sintering machine in full-melting mode. The levels of the processing factors (Table 2) have been assessed in a previous optimization, aimed at reducing the overall porosity and improving the surface quality of the as-built
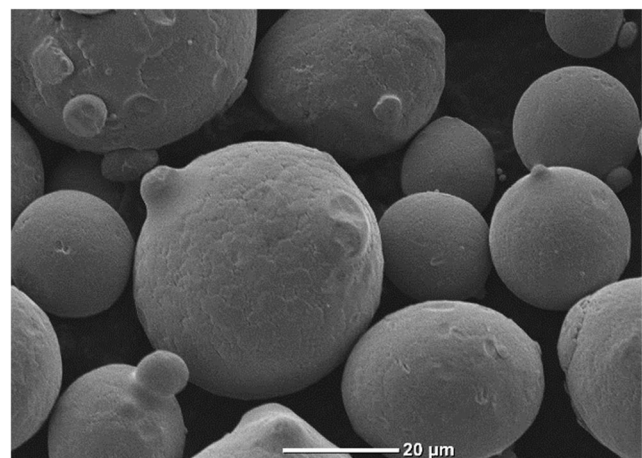

Fig. 1 SEM inspection of virgin powder at 1000× magnification

Table 1 EOS GP1 powder, nominal chemical composition (wt.%); single values to be intended as maximum

Cr	Ni	Cu	Mn	Si	Mo	Nb	C	Fe
15.0 ÷ 17.5	3 ÷ 5	3 ÷ 5	1	1	0.5	0.15 ÷ 0.45	0.07	Balanced

products. Since a 20-μm layer thickness has been set, 3000 layers have been required to manufacture the samples in the selected direction of growth (Fig. 2). To enhance the densification of the powder, each layer has been exposed with adjacent laser traces with partial overlapping: these are spaced with the preset hatch distance, and the direction of scanning has been rotated by 67° between consecutive layers, in order to promote mutual adhesion.

2.2 Laser beam welding

A solid-state disc laser has been used for LBW (Table 3), with a 6-axis robot to move the laser head. The welding line (Fig. 3) has been equipped with a patented device [28], supplying Ar shielding at 25 L/min to prevent oxidation at the top- and back-side and He at 30 L/min to remove the plasma plume. A 3-factor, 3-level, full factorial experimental plan has been arranged (Table 4) involving laser power P, laser speed s, and defocusing z, resulting in 27 testing conditions, with 3 replications each. The weld has been performed along the side orthogonal to the growth direction in LPBF. No filler metal has been considered; therefore, welding has been performed as autogenous.

The geometry of the beads in the cross-section has been investigated via light microscopy upon cutting, grinding, mirror polishing, and chemical etching; namely, the width w_t at the top-side, the width w_b at the back-side, and the extent of the fusion zone FZ have been measured (Fig. 4). Also, the welding imperfection undercut UC, excessive metal EM, and shrinkage groove SG, each one at the top- and down-side, have been considered (Fig. 5) and compared to the corresponding allowed threshold as defined by the referred standard [27].

Fig. 2 Additive manufacturing of the specimens for welding

Vickers micro-hardness testing [29] has been conducted to evaluate the extent of the heat-affected zone (HAZ), performing a pattern of indentations at mid-height, with a load of 300 gf for a dwell time of 10 s; a step of 120 μm has been allowed between consecutive indentations. Eventually, tensile testing has been conducted in agreement with ASTM standards [30]; the specimens (Fig. 6) have been obtained with laser cutting of larger welded plates, 3 mm thick as for the samples of the experimental campaign. To improve the elastic modulus, the ultimate tensile strength, the yield strength, and the ductility of the material, heat treating is strongly suggested in the literature [11]: to this purpose, as-built and welded specimens have been heat treated at 650 °C for 1 h, in vacuum.

3 Results and discussion

3.1 Visual inspection and geometry

At first, visual inspections (Table 5) have been conducted: since the welding beads are uniform and smooth, shielding is deemed effective; cracks neither spattering resulted. Then, the transverse cross-sections have been inspected (Table 6).

Based on the shape of the fusion zone in the cross-section, the position of the laser focus clearly rules the welding mode:

Table 2 Levels of the governing factors for AM in full-melting mode

Parameter	Value
Operating laser power [W]	195
Operating wavelength [nm]	1030
Linear scanning speed [m·s^{-1}]	1.2
Hatch distance [mm]	0.09
Layer thickness [mm]	0.02
Focused laser diameter [mm]	0.09

Table 3 Main features of the solid-state disc laser for LBW

Parameter	Value
Maximum operating power [kW]	4.0
Operating wavelength [nm]	1030
Beam parameter product [mm·mrad]	12.0
Core diameter of the delivering fiber [mm]	0.300
Focus diameter [mm]	0.300

Fig. 3 System set-up for LBW

Fig. 4 Scheme of the geometrical responses in the cross-section of the welding bead
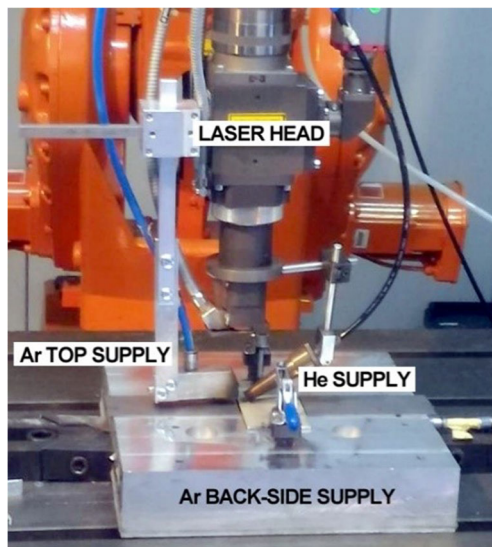
namely, when shifting from positive to negative defocusing, the process moves from conduction mode to key-hole mode; consequently, the resulting welding mode depends on the condition of processing. To further discuss the geometry, the responses have been measured and averaged among the replications (Table 7); instead, the maximum value for each welding imperfections has been considered to apply a global quality label, according to the referred standard [27].

Multiple random cross-sections of the welds have been examined to check the quality level even in terms of possible pores. Local occurrence of micropores not exceeding 10-μm size must be reported (Fig. 7), although the referred standards [27] are matched in terms of individual equivalent diameter and cumulated pore area.

The conditions producing lack of fusion or incomplete penetration have been excluded from further consideration; all the remaining comply with standards at the intermediate level at least, therefore have been used to develop the response surfaces to feed the optimization in the following section.

3.2 Microstructure and micro-hardness

The microstructure of the base metal prior to welding is significantly different from the microstructure of a wrought steel of the same chemical composition. Indeed, the wave-shaped,

overlapping melting pools are visible (Fig. 8) as a result of the building strategy consisting in adjacent, partially overlapping traces and multiple exposures for each layer. In detail, an austenitic matrix of parallel columnar grains, with minor fractions of irregular martensite, is observed (Fig. 9): this is the peculiar microstructure resulting upon LPBF, when the atomization of the virgin powder is conducted in nitrogen atmosphere [31–33], as for the powder of the experimental plan; a fully martensitic structure would result in case of argon atomization, instead [34].

Since the base metal experiences fusion and solidification due to welding, the original microstructure is lost, although the features of the new grains in the fusion zone are independent on the welding mode. More specifically, based on the geometry of the fusion zone, it has been discussed that shifting from positive to negative defocusing results in moving from conduction mode to key-hole mode, although both lead to the same microstructure in the fusion zone (Figs. 10 and 11).

Namely, austenite is retained as the main phase in the welding bead, where elongated grains are found in the direction of the heat flow, hence from the center of the seam
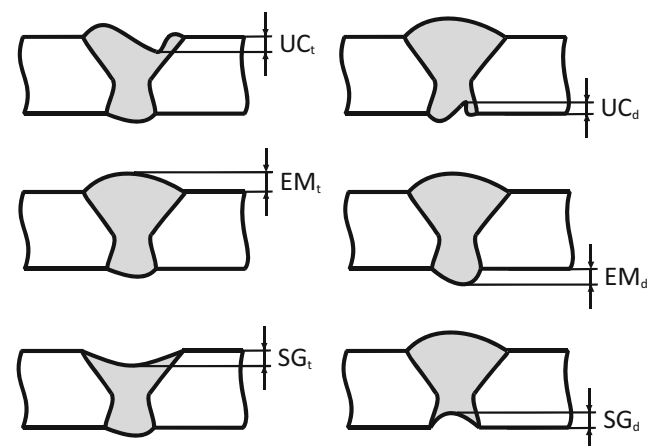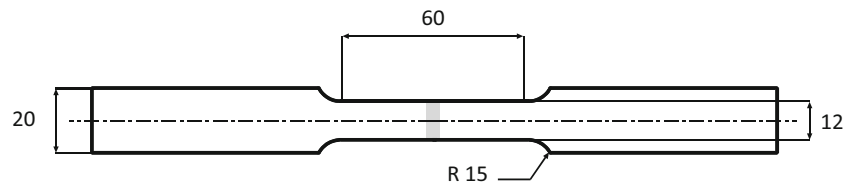
Table 4   Levels of the governing factors of the experimental plan

	Minimum	Center	Maximum
Laser power [kW]	1.5	2.5	3.5
Laser speed [mm·s^{-1}]	25	35	45
Defocusing [mm]	−2.5	0.0	+2.5

Fig. 5 Scheme of the imperfections in the cross-section of the welding bead, top- and down-side

Fig. 6 Tensile specimen according to ASTM standard, dimensions in millimeters

towards the base material (Figs. 12 and 13); annealing is thought to occur in the HAZ [35], instead, with coarsening of Cu-rich dispersed precipitates [32], ascribed to heating from the fusion zone (Fig. 14).

Different microstructures in the regions of interest are reasons for different micro-hardness, in agreement with the literature, where it has been proved that higher percentages of retained austenite yield a reduction of strength and hardness

Table 5 Surface aspects of the top-side of the welding bead for each condition of processing

Processing conditions		Defocusing −2.5 mm	Focused beam	Defocusing +2.5 mm
1.5 kW	25 mm·s^{-1}			Excluded due to lack of fusion
	35 mm·s^{-1}			Excluded due to lack of fusion
	45 mm·s^{-1}		Excluded due to lack of fusion	Excluded due to lack of fusion
2.5 kW	25 mm·s^{-1}			
	35 mm·s^{-1}			Excluded due to lack of fusion
	45 mm·s^{-1}			Excluded due to lack of fusion
3.5 kW	25 mm·s^{-1}			
	35 mm·s^{-1}			
	45 mm·s^{-1}			

Table 6 Cross-sections of the welding bead for each condition of processing
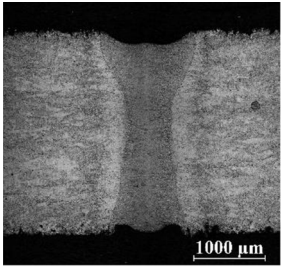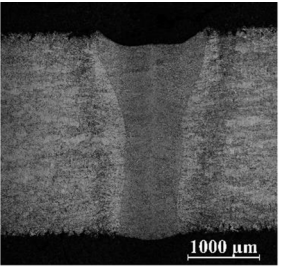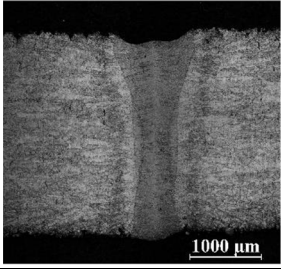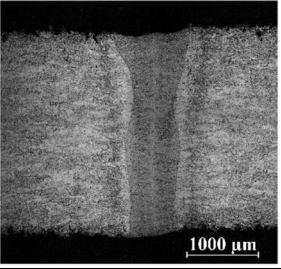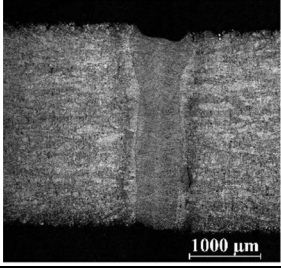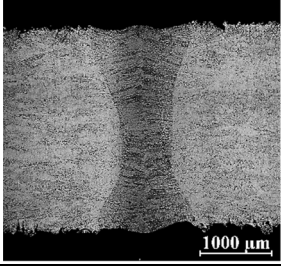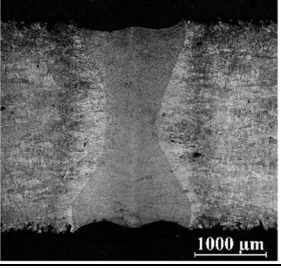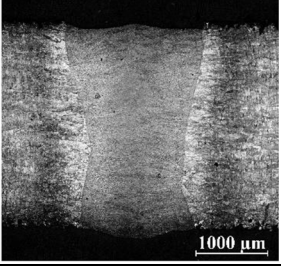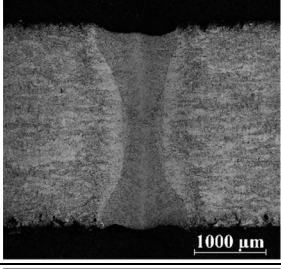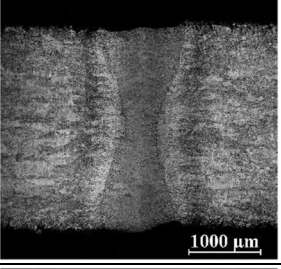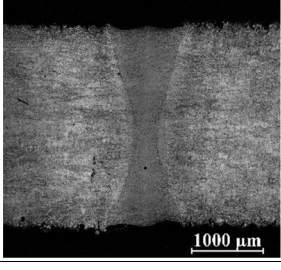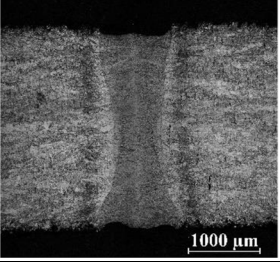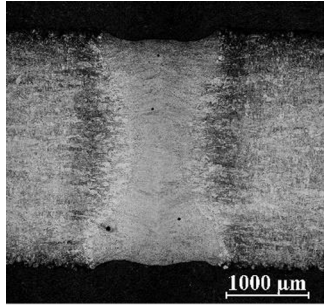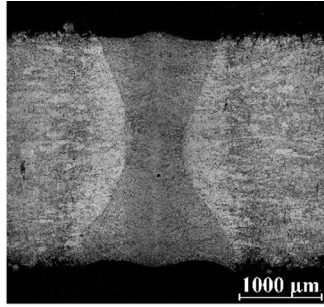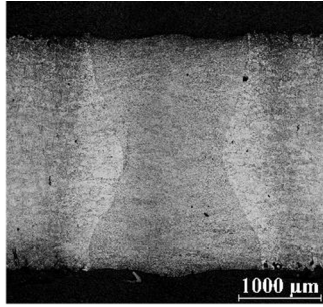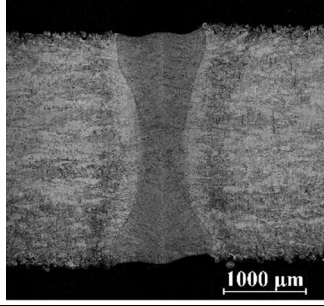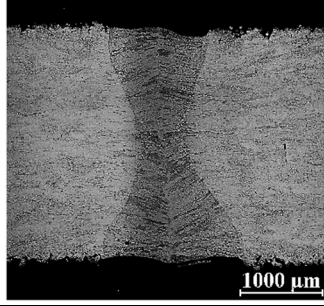
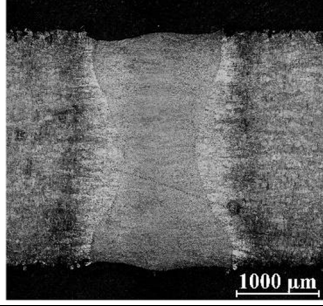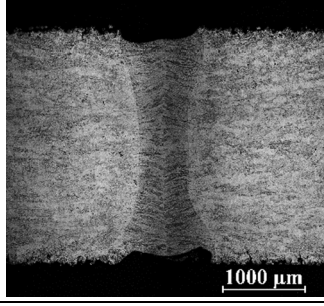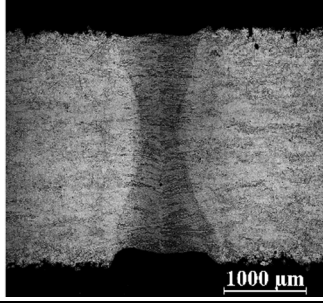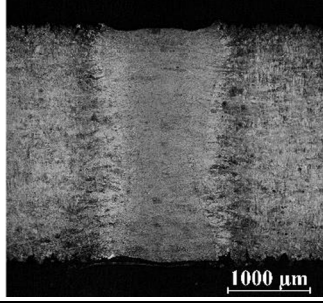| Processing conditions		Defocusing −2.5 mm	Focused beam	Defocusing +2.5 mm
1.5 kW	25 mm·s⁻¹			Excluded due to lack of fusion
	35 mm·s⁻¹			Excluded due to lack of fusion
	45 mm·s⁻¹		Excluded due to lack of fusion	Excluded due to lack of fusion
2.5 kW	25 mm·s⁻¹			
	35 mm·s⁻¹			Excluded due to lack of fusion
	45 mm·s⁻¹			Excluded due to lack of fusion

Table 6   (continued)

[36]. Therefore, based on the trend of Vickers micro-hardness at mid-height (Fig. 15), the extent of the HAZ can be inferred for each condition (Table 8). A drop of micro-hardness in a measure of 16 and 10% on average is experienced in the FZ and the HAZ, respectively, compared with the base metal. The reduction of hardness upon fusion and re-solidification has been observed even after laser surface modification of the same alloy [37]. Interestingly, the average micro-hardness is not affected by the levels of the processing factors, because the same phenomena of grain refinement and retention of austenite occur, irrespectively of the welding mode, as stated when discussing the microstructure.

3.3 Response surfaces

With stepwise regression [38], the equations of the response surfaces have been found. It is worth noting that, in agreement with previous research works about LBW of metals [25], imperfections exhibit a pure random nature; therefore, any predicting model is not significant. Instead, the approach proved effective for the geometrical responses (Table 9).

Namely, in terms of the normalized factors in the range [−1, +1], the following equations resulted:

$$W_t = 1.3 + 0.1P - 0.3s + 0.3z + 0.1Ps - 0.2P^2 + 0.2z^2$$

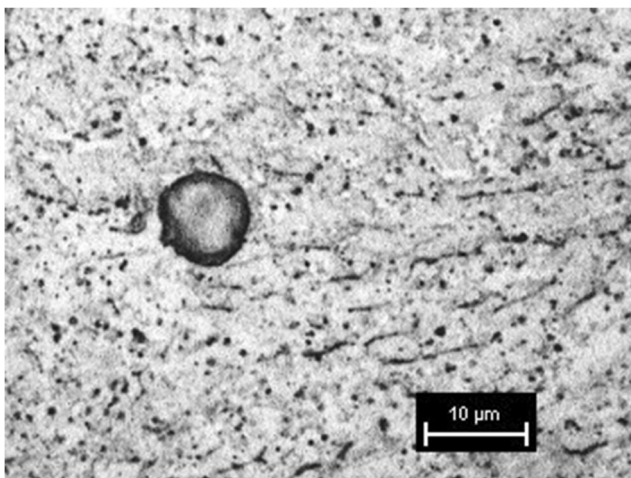$$W_d = 1.4 + 0.5P - 0.3s + 0.2Ps - 0.1P^2 - 0.2z^2$$

$$FZ = 2.6 + 0.2P - 0.6s + 0.8z - 0.2sz - 0.2P^2 + 0.5z^2$$

$$HAZ = 1.8 + 0.1P - 0.4s + 0.5z$$

A same global trend is found. Namely, in agreement with intuitive expectation, each response decreases with speed and increases with laser power, i.e., any increase of energy input yields a proportional increase of fusion (Fig. 16). As suggested by the shape of the fusion zone in the cross-section, negative defocusing yields a shift from conduction mode to key-hole mode; consequently, part of the laser irradiance is lost to produce vaporization to start the key-hole; therefore, the extent of the fusion zone is comparatively reduced.

Table 7 Average geometrical responses and maximum imperfections in the cross-section

Processing conditions			Geometrical responses			Imperfections						
P [kW]	s [mm·s⁻¹]	z [mm]	W_t [mm]	W_d [mm]	FZ [mm²]	UC_t [mm]	UC_d [mm]	EM_t [mm]	EM_d [mm]	SG_t [mm]	SG_d [mm]	ISO quality
1.5	25	− 2.5	1.35	1.00	2.36	–	0.10	–	0.04	0.25	–	Severe (B)
		0.0	1.40	0.97	2.63	–	0.12	–	0.06	0.19	–	Severe (B)
		+ 2.5	Excluded due to lack of fusion									
	35	− 2.5	1.03	0.64	2.02	–	0.06	–	0.15	0.16	–	Severe (B)
		0.0	0.78	0.88	2.04	–	0.08	–	0.10	0.26	–	Severe (B)
		+ 2.5	Excluded due to lack of fusion									
	45	− 2.5	0.83	0.55	1.76	–	0.06	–	0.10	0.19	–	Severe (B)
		0.0	Excluded due to lack of fusion									
		+ 2.5										
2.5	25	− 2.5	1.45	1.30	2.75	0.16	0.17	–	0.07	–	–	Interm. (C)
		0.0	1.53	1.76	3.24	0.17	0.18	–	–	–	–	Interm. (C)
		+ 2.5	2.23	1.35	4.78	0.12	–	–	0.20	–	–	Severe (B)
	35	− 2.5	0.99	1.19	2.16	–	0.13	–	–	0.15	–	Severe (B)
		0.0	1.17	1.21	2.52	0.15	0.12	0.12	0.10	–	–	Interm. (C)
		+ 2.5	Excluded due to lack of fusion									
	45	− 2.5	1.02	0.92	1.88	–	0.13	–	–	0.14	0.20	Severe (B)
		0.0	1.05	1.17	2.15	–	0.13	–	–	0.14	–	Severe (B)
		+ 2.5	Excluded due to lack of fusion									
3.5	25	− 2.5	1.34	1.58	2.75	0.19	0.16	–	–	–	–	Interm. (C)
		0.0	1.40	1.86	3.35	0.12	0.15	–	–	–	–	Severe (B)
		+ 2.5	1.92	2.10	4.65	0.10	0.04	–	0.13	–	–	Severe (B)
	35	− 2.5	1.09	1.22	2.27	0.14	0.12	–	–	–	–	Severe (B)
		0.0	1.21	1.69	2.84	0.12	0.16	–	–	–	–	Interm. (C)
		+ 2.5	1.57	1.73	3.81	0.14	0.06	–	0.14	–	–	Severe (B)
	45	− 2.5	0.92	1.04	1.95	0.19	0.26	–	–	–	–	Interm. (C)
		0.0	1.07	1.33	2.28	0.14	0.13	–	–	–	0.24	Severe (B)
		+ 2.5	1.42	1.36	3.24	0.16	0.08	–	–	–	0.19	Interm. (C)

3.4 Optimization

The numerical optimization has been conducted with the method of the desirability function, which is widely used in both research and industrial applications when multiple

Fig. 7 Detail of a micropore for the processing condition with 1.5 kW, 25 mm·s⁻¹, −2.5 mm
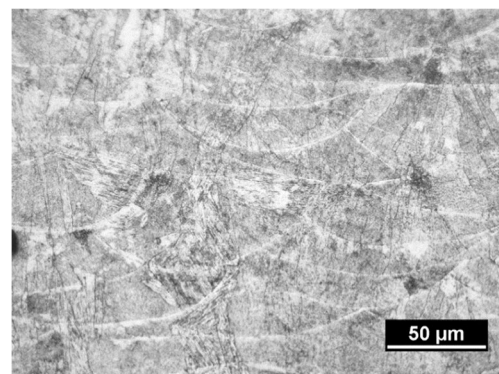
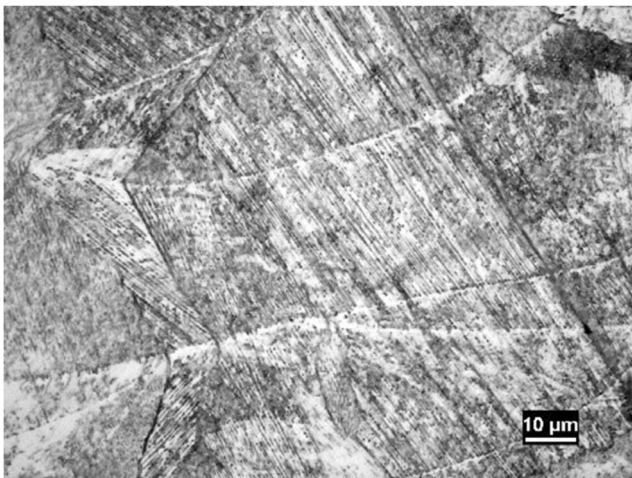**Fig. 8** Microstructure of the base metal: wave-shaped pools due to exposure strategy

Fig. 9 Microstructure of the base metal: parallel columnar grains in the austenitic matrix
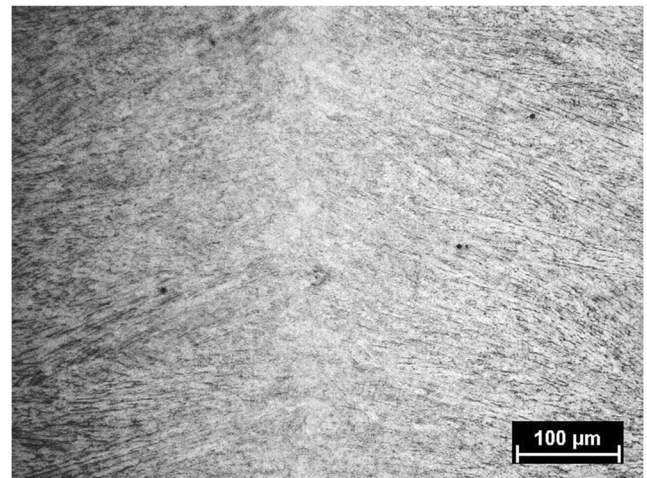

Fig. 12 Microstructure in the fusion zone: symmetry of the grains along the center line of the seam for the processing condition with 1.5 kW, 25 mm·s^{-1}, −2.5 mm
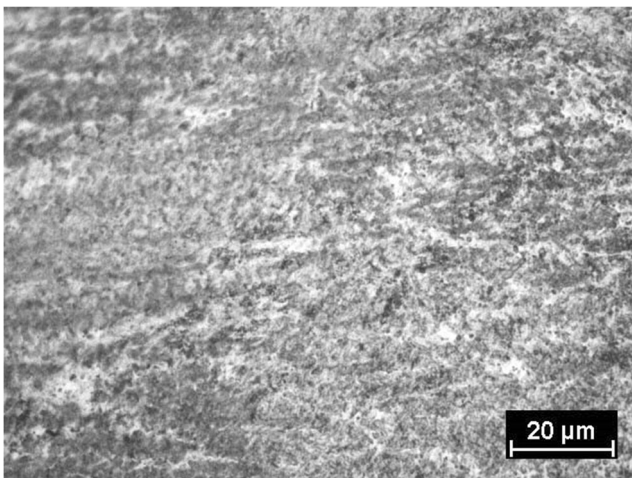

Fig. 10 Detail of the microstructure in the fusion zone for the processing condition with 2.5 kW, 25 mm·s^{-1}, +2.5 mm resulting in conduction mode welding
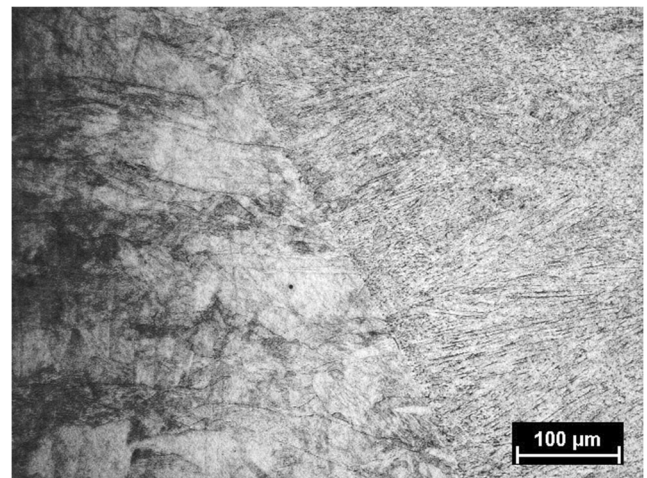

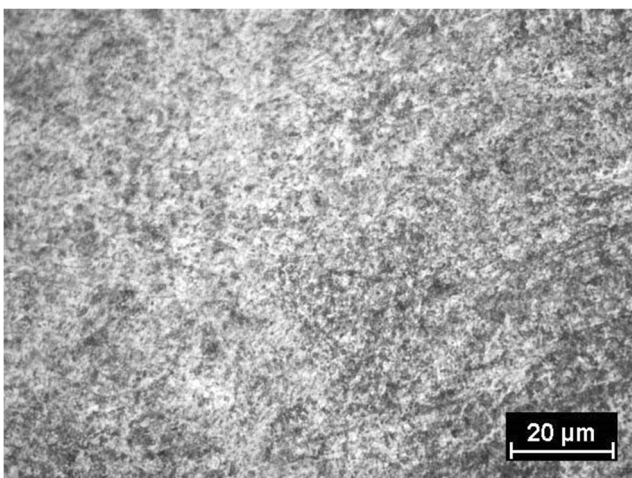**Fig. 13** Microstructure at the interface between fusion zone and HAZ for the processing condition with 1.5 kW, 25 mm·s^{-1}, −2.5 mm

Fig. 11 Detail of the microstructure in the fusion zone for the processing condition with 2.5 kW, 25 mm·s^{-1}, −2.5 mm resulting in key-hole mode welding
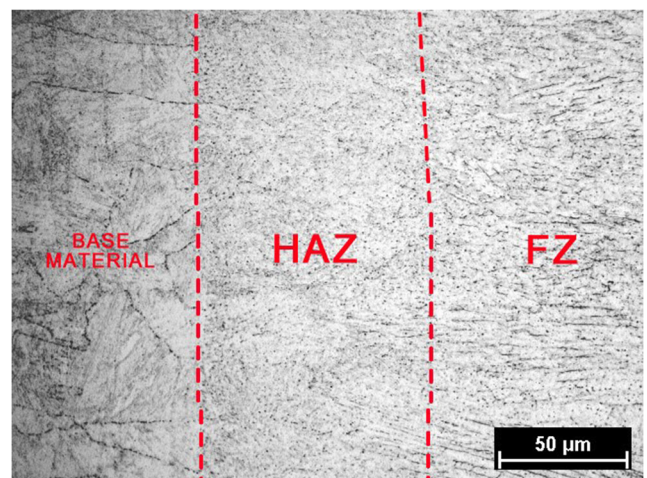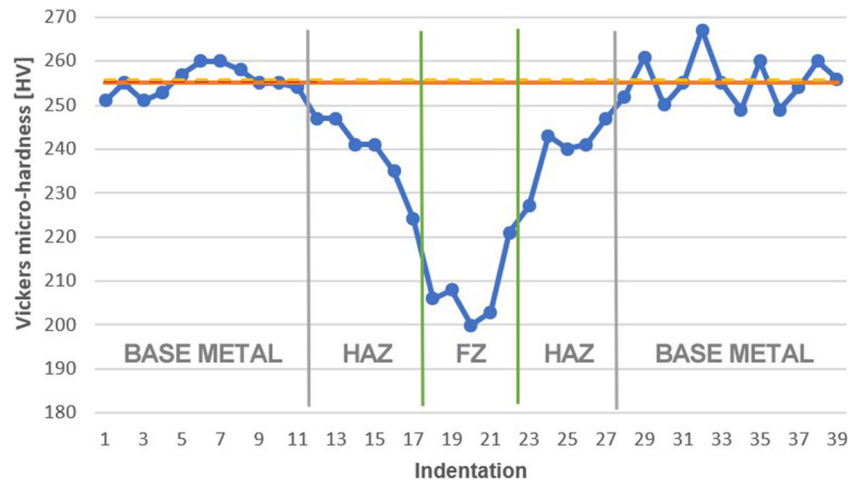

Fig. 14 Microstructures in base material, HAZ, and fusion zone for the processing condition with 1.5 kW, 25 mm·s^{-1}, −2.5 mm

Fig. 15 Example of the trend of Vickers micro-hardness for the processing condition with 1.5 kW, 25 mm·s⁻¹, −2.5 mm

responses must be combined into an overall function. Basically, each response is given an individual desirability value d_i between 0 and 1, representing a completely undesirable value or the best possible value, respectively, towards the intended goal; when all the responses are given the same importance, the global desirability D is evaluated as geometrical mean of individual desirability values:

$$D = \sqrt[n]{d_1 \cdot d_2 \cdots \cdots d_n}$$

Therefore, the dependence on the processing factor is inherited by the response surface of the global desirability. Eventually, the optimum is selected as the solution whose global desirability approaches 1. The goal of minimization has been imposed to FZ and HAZ; moreover, the ratio of the top width to down width has been targeted to 1, aiming at preferring a typical key-hole shape with deep and complete penetration through the material thickness and concurrent reduced affection in terms of width. Equal importance has been awarded to each constraint; therefore, the usual formula for the geometrical mean applies.

The response surface of the desirability function (Fig. 17) presents a maximum of 97% for laser power of 2.1 kW, speed of 45 mm/s, and a negative defocusing of 1.5 mm, which is suggested as the optimum for processing; the solution is robust since the desirability is stable around its maximum (Table 10).

Then, LBW has been performed in the suggested condition to check the reliability of the regression equations (Table 11): namely, an average prediction error below 7% is found; moreover, the standards for the imperfections are matched at the intermediate level quality.

Table 8 Extent of the HAZ and mean values of Vickers micro-hardness for full-penetrative welding conditions

Processing conditions			HAZ extent [mm]	Micro-hardness	
P [kW]	s [mm·s⁻¹]	z [mm]		In HAZ	In FZ
1.5	25	− 2.5	1.80	239	208
		0.0	2.04	238	219
	35	− 2.5	1.32	238	216
		0.0	1.44	239	206
	45	− 2.5	1.20	243	209
2.5	25	− 2.5	1.68	234	214
		0.0	2.40	229	220
		+ 2.5	2.52	231	218
	35	− 2.5	1.08	233	212
		0.0	1.80	242	223
	45	− 2.5	0.96	235	209
		0.0	1.56	233	214
3.5	25	− 2.5	2.16	243	211
		0.0	2.04	234	219
		+ 2.5	3.00	237	215
	35	− 2.5	1.44	235	212
		0.0	1.92	237	212
		+ 2.5	2.40	242	223
	45	− 2.5	1.08	233	214
		0.0	1.56	233	208
		+ 2.5	2.04	234	213

Table 9 Determination coefficients R-squared and p-values of each response surface

	R-squared	Adjusted R-squared	p-value
Top width W_t	0.9379	0.9113	< 0.0001
Down width W_d	0.9540	0.9342	< 0.0001
Fused zone FZ	0.9799	0.9713	< 0.0001
Extent of the HAZ	0.8997	0.8821	< 0.0001

Fig. 16 Response surface of the extent of the fusion zone as a function of speed and defocusing for a given power of 2.5 kW
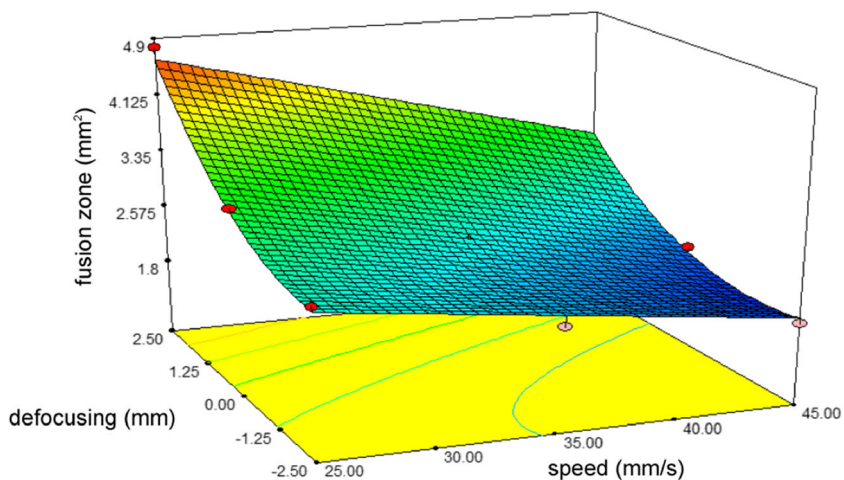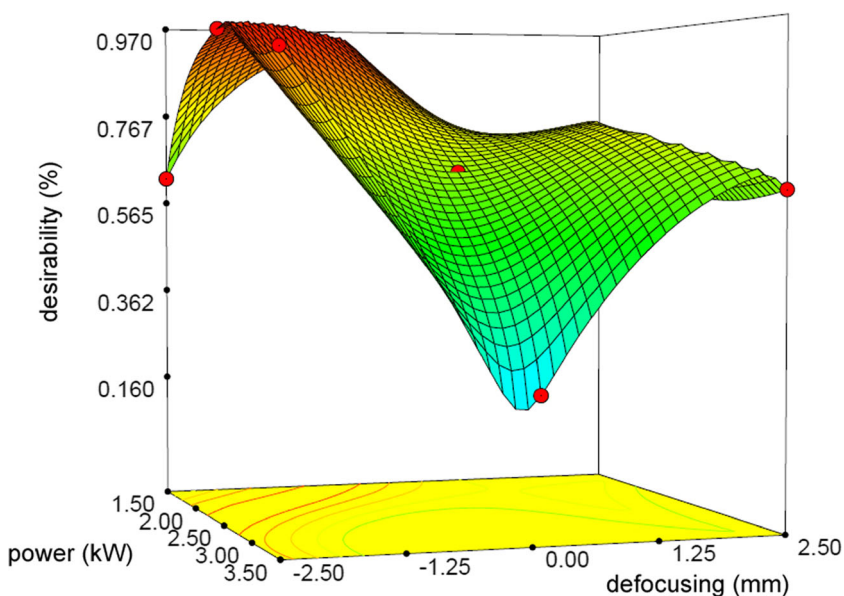

Fig. 17 Response surface of the global desirability function for a given speed of 45 mm·s^{-1}

3.5 Tensile tests

The final validation of the optimum has been conducted upon tensile testing, in comparison with the unwelded AM counterpart, which is the proper benchmark to consider. Indeed, the observed mainly austenitic microstructure resulting from LPBF is significantly different from the fully martensitic microstructure obtained in wrought or casted material of the same composition [32].

Three as-built and six welded specimens have been tested; a regression with the method of least squares has been used to fit the data in the elastic stage and evaluates the elastic modulus; the yield strength at 0.2% strain offset has been referred.

Table 10 Global desirability for the first five processing conditions suggested by the numerical optimization

P [kW]	s [mm·s^{-1}]	z [mm]	Desirability
2.09	45	− 1.55	0.971
2.10	45	− 1.57	0.971
2.12	45	− 1.61	0.971
2.07	45	− 1.50	0.971
2.06	45	− 1.48	0.971

Table 11 Actual vs. predicted values of each predicted response

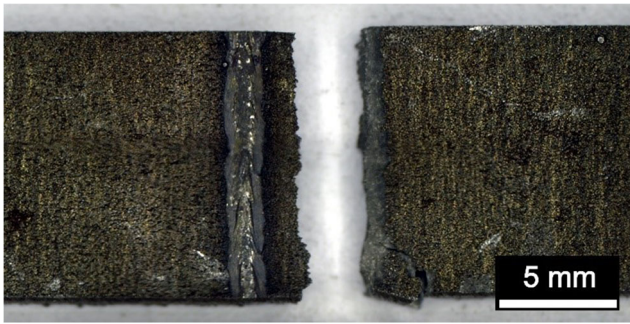|	Predicted	Actual	Percentage error
Top width W_t [mm]	0.72	0.68	5.9%
Down width W_d [mm]	0.85	0.79	7.6%
Fused zone FZ [mm^2]	1.78	1.63	9.2%
Extent of the HAZ [mm]	1.12	1.08	3.7%

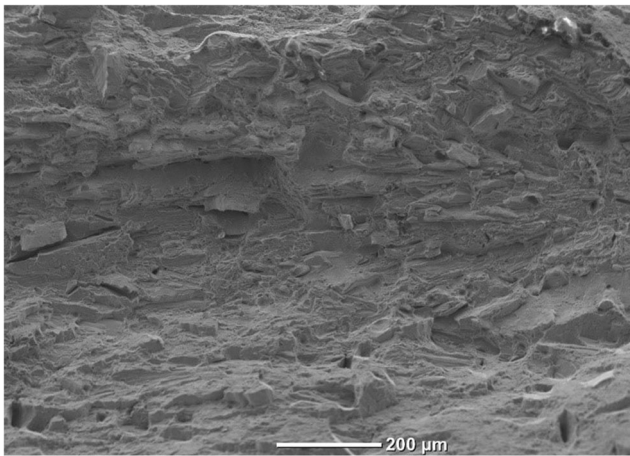**Fig. 18** Sample of a fractured welded specimen

Fig. 19 Surface fracture of the as-built sample

Fractures are located in the calibrated length, outside of the welding area (Fig. 18); it is inferred that martensite is produced under loading, thanks to transformation-induced plasticity [39]. Consequently, the same fracture surfaces are found for the as-built and the welded
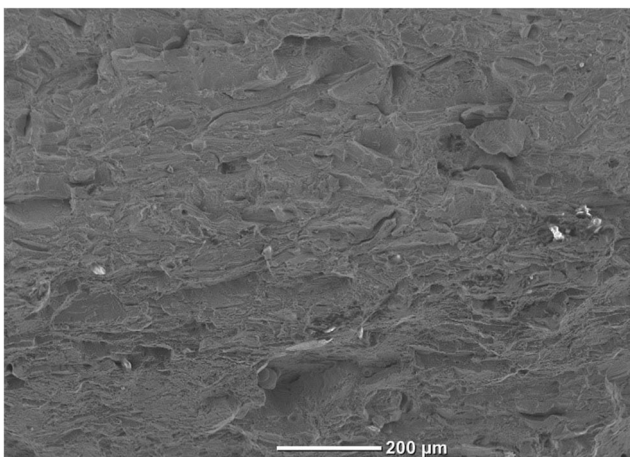

Fig. 20 Surface fracture of the welded sample, with fracture locating outside of the welding bead
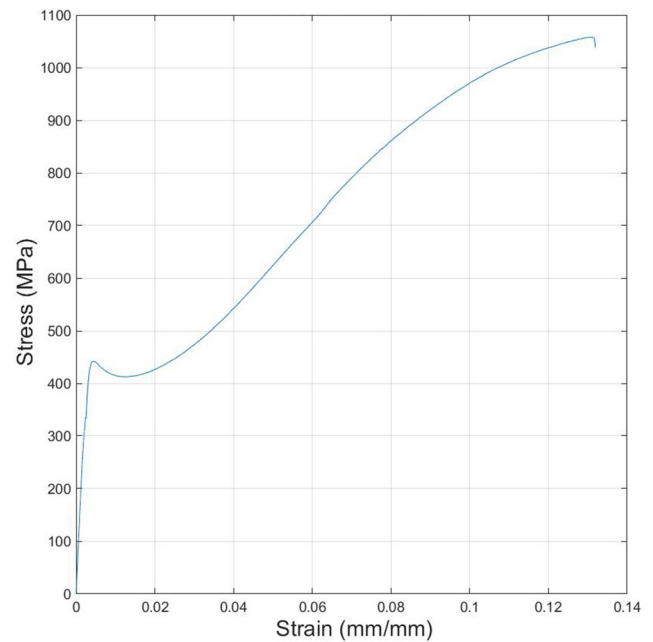
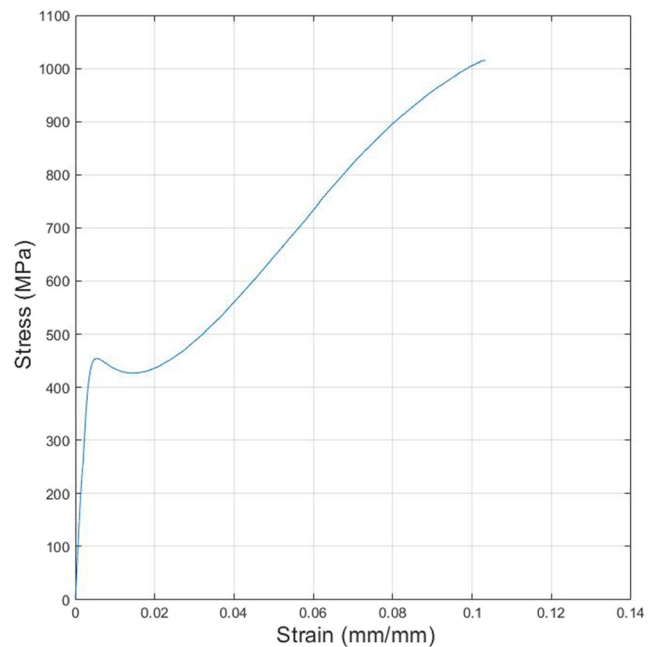

Fig. 21 Stress-strain diagram of an as-built specimen

Fig. 22 Stress-strain diagram of a welded specimen

Table 12 Mechanical properties of wrought material as given by ASM handbook and tested as-built specimens

	Elastic modulus [GPa]	Yield strength [MPa]	UTS [MPa]	Ductility [%]
Wrought material	**190–210**	**1170**	**1310**	**10**
As-built specimen 1	158	428	984	9
As-built specimen 2	142	461	1055	12
As-built specimen 3	128	433	1050	13
Average	143	441	1030	11
Standard deviation	12	15	32	2

Table 13 Mechanical properties of welded specimens

	Elastic modulus [GPa]	Yield strength [MPa]	UTS [MPa]	Ductility [%]
Welded sample 1	168	447	1058	11
Welded sample 2	124	454	1020	10
Welded sample 3	137	460	1052	10
Welded sample 4	161	449	1050	10
Welded sample 5	155	461	1025	10
Welded sample 6	160	462	1081	11
Average	151	456	1048	10
Standard deviation	15	6	20	0

specimens (Figs. 19 and 20). Interestingly, even the same trend of stress-strain has been found (Figs. 21 and 22), with convincing matching for average elastic modulus, yield strength, ultimate tensile strength, and ductility (Tables 12 and 13); namely, there is no statistical difference among the two groups at a level of significance of 95%.

4 Conclusions

Based on a structured factorial plan and extracting the response surfaces of the geometry of the welding bead, convincing findings have been presented in this paper regarding the issue of joining metal parts manufactured by means of laser powder bed fusion. Namely, the following main findings can be highlighted:

- The known advantages of laser beam welding are benefited to comply with usual international standards.
- An optimum condition to weld 3-mm-thick plates has been found, based on the consolidated method of the desirability function, and tested.
- The same mechanical properties of the unwelded (i.e., as-built) part have been found.

Further tests must be conducted to extend this approach to more complex welding paths of different thickness; the same approach can be considered to define the constraints and find the optimum.

Declarations

References

1. ASTM International (2015) ISO / ASTM 52900:2015, Additive manufacturing — General principles — Terminology. ASTM International, West Conshohocken, pp 1–19
2. Paoletti I (2017) Mass customization with additive manufacturing: new perspectives for multi performative building components in architecture. Procedia Eng 180:1150–1159
3. Qiang L, Kucukkoc I, Zhang D (2017) Production planning in additive manufacturing and 3D printing. Comput Oper Res 83: 157–172
4. Garcia-Colomo A, Wood D, Martina F, Williams WS (2020) A comparison framework to support the selection of the best additive manufacturing process for specific aerospace applications. Int J Rapid Manuf 9(2/3):194–211
5. Caiazzo F, Alfieri V, Corrado G, Argenio P (2017) Laser powder-bed fusion of Inconel 718 to manufacture turbine blades. Int J Adv Manuf Technol 93:4023–4031
6. Caiazzo F, Cardaropoli F, Alfieri V, Sergi V, Cuccaro L (2013) Experimental analysis of selective laser melting process for Ti-6Al-4V turbine blade manufacturing. In: XIX International Symposium on High-Power Laser Systems and Applications, Istanbul
7. Usera D, Alfieri V, Caiazzo F, Argenio P, Corrado G, Ares E (2017) Redesign and manufacturing of a metal towing hook via laser additive manufacturing with powder bed. Procedia Manuf 13:825–832
8. Prashanth K, Damodaram R, Maity T, Wang P, Eckert J (2017) Friction welding of selective laser melted Ti6Al4V parts. Mater Sci Eng A 704:66–71
9. Sun Y, Wang P, Lu S, Li L, Nai M, Wei J (2019) Laser welding of electron beam melted Ti-6Al-4V to wrought Ti-6Al-4V: effect of welding angle on microstructure and mechanical properties. J Alloys Compd 782:967–972
10. Wang H, Zhang S, Wang X (2009) Progress and challenges of laser direct manufacturing of large titanium structural components. Chin J Lasers 36(12):3204–3209

11. Rafi H, Pal D, Patil N, Starr T, Stucker B (2014) Microstructure and mechanical behavior of 17-4 precipitation hardenable steel processed by selective laser melting. J Mater Eng Perform 23:4421–4428

12. Thijs L, Kempen K, Kruth J, Humbeecs J (2013) Fine-structured aluminium products with controllable texture by selective laser melting of pre-alloyed AlSi10Mg powder. Acta Mater 61:1809–1819

13. Du Z, Chen H, Tan M, Bi G, Chua C (2018) Investigation of porosity reduction, microstructure and mechanical properties for joining of selective laser melting fabricated aluminium composite via friction stir welding. J Manuf Process 36:33–43

14. Prashanth K, Damodaram R, Scudino S, Wang Z, Rao K, Eckert J (2014) Friction welding of Al–12Si parts produced by selective laser melting. Mater Des 57:632–637

15. Blackburn J (2012) Laser welding of metals for aerospace and other applications. In: Welding and joining of aerospace materials. Woodhead Publishing Series in Welding and Other Joining Technologies, Cambridge, pp 75–108

16. Steen W, Mazumder J (2003) Laser material processing. Springer, Berlin

17. Caiazzo F, Caggiano A (2018) Investigation of laser welding of Ti alloys for cognitive process parameters selection. Materials 11:632–642

18. Nahmany M, Rosenthal I, Benishti I, Frage N, Stern A (2015) Electron beam welding of AlSi10Mg workpieces produced by selected laser melting additive manufacturing technology. Addit Manuf 8:63–70

19. Chen X, Zhang J, Cheng X, Huang Z (2018) Electron beam welding of laser additive manufacturing Ti-6.5Al-3.5Mo-1.5Zr-0.3Si titanium alloy thick plate. Vacuum 158:116–121

20. Kuryntsev S (2018) The influence of pre-heat treatment on laser welding of T-joints of workpieces made of selective laser melting steel and cold rolled stainless steel. Opt Laser Technol 107:59–66

21. Matilainen V, Pekkarinen J, Salminen A (2016) Weldability of additive manufactured stainless steel. Phys Procedia 83:808–817

22. Wits W, Becker JJ (2015) Laser beam welding of titanium additive manufactured parts. Procedia CIRP 28:70–75

23. Yu H, Li F, Yang J, Shao J, Wang Z, Zeng X (2018) Investigation on laser welding of selective laser melted Ti-6Al-4V parts: weldability, microstructure and mechanical properties. Mater Sci Eng A 712:20–27

24. Hu X, Xue Z, Zhao G, Yun J, Shi D, Yang X (2019) Laser welding of a selective laser melted Ni-base superalloy: microstructure and high temperature mechanical property. Mater Sci Eng A 745:335–345

25. Caiazzo F, Alfieri V, Sergi V, Schipani A, Cinque S (2013) Dissimilar autogenous disk-laser welding of Haynes 188 and Inconel 718 superalloys for aerospace applications. Int J Adv Manuf Technol 68:1809–1820

26. Kawahito Y, Mizutani M, Katayama S (2007) Investigation of high power fiber laser welding phenomena of stainless steel. Trans Join Weld Res Inst 36(2):11–16

27. International Organization for Standardization (2019) ISO 13919-1: 2019 - Electron and laser-beam welded joints — requirements and recommendations on quality levels for imperfections — Part 1: Steel, nickel, titanium and their alloys, pp 1–15

28. Caiazzo F, Sergi V, Corrado G, Alfieri V, Cardaropoli F (2015) Automated apparatus of laser beam welding. Patent EP2, 931, 468(A1)

29. International Organization for Standardization (2005) ISO 6507-1: 2005 - Metallic materials — Vickers hardness test — Part 1: Test method, pp 1–19

30. ASTM International (2016) ASTM E8 / E8M-16a - Standard test methods for tension testing of metallic materials, pp 1–30

31. Contaldi V, Del Re F, Palumbo B, Squillace A, Corrado P, Di Petta P (2019) Mechanical characterisation of stainless steel parts produced by direct metal laser sintering with virgin and reused powder. Int J Adv Manuf Technol 109:3337–3351

32. Al Mangour B, Yang J (2017) Understanding the deformation behavior of 17-4 precipitate hardenable stainless steel produced by direct metal laser sintering using micropillar compression and TEM. Int J Adv Manuf Technol 90:119–126

33. Gu H, Gong H, Pal D, Rafi K, Starr T, Stucker B (2013) Influences of energy density on porosity and microstructure of selective laser melted 17-4PH stainless steel. In: 24th Annual International Solid Freeform Fabrication Symposium

34. Murr L, Martinez E, Hernandez J, Collins S, Amato K, Gaytan S, Shindo P (2012) Microstructures and properties of 17-4 PH stainless steel fabricated by selective laser melting. J Mater Res Technol 1(3):167–177

35. Vander Voort G, Lucas G, Manilova E (2014) Metallography and microstructures of stainless steels and maraging steels. In: ASM Handbook 9—Metallography and Microstructures. ASM International, Materials Park

36. Zai L, Zhang C, Wang Y, Guo W, Wellmann D, Tong X, Tian Y (2020) Laser powder bed fusion of precipitation-hardened martensitic stainless steels: a review. Metals 10(255):1–25

37. Alfieri V, Argenio P, Caiazzo F, Sergi V (2017) Reduction of surface roughness by means of laser processing over additive manufacturing metal parts. Materials 10(30):1–12

38. Montgomery D (2005) Design and analysis of experiment. McGraw Hill, New York

39. Clausen B, Brown D, Carpenter J, Clarke K, Clarke A, Vogel S, Bernardin J, Spernjak D, Thompson J (2017) Deformation behavior of additively manufactured GP1 stainless steel. Mater Sci Eng A 696:331–340